Structural and functional properties of Zn(Ge,Sn)N2 thin films deposited by reactive sputtering

Nicole Beddelem, Stéphanie Bruyere, Franck Cleymand, Sebastien Diliberto, Christophe Longeaud, Sylvain Le Gall, Roselyne Templier, Patrice Miska, Bérangère Hyot

Version of Record: https://www.sciencedirect.com/science/article/pii/S0040609020304028
Manuscript_667558a0f89015d263344382c8fd034b

Structural and functional properties of $Zn(Ge,Sn)N_2$ thin films deposited by reactive sputtering

Nicole Beddelem[a,b], Stéphanie Bruyère[b], Franck Cleymand[b], Sébastien Diliberto[b], Christophe Longeaud[c], Sylvain le Gall[c], Roselyne Templier[a], Patrice Miska[b] and Bérangère Hyot[a,*]

[a]*Univ. Grenoble Alpes, CEA, LETI, F-38000 Grenoble, France*

[b]*Univ. de Lorraine, CNRS, IJL, F-54000 Nancy, France*

[c]*GEEPS (UMR 8507 CNRS), Centrale-Supélec, Université Paris Sud XI, Université Pierre et Marie Curie, 91190 Gif sur Yvette, France*

**corresponding author: berangere.hyot@cea.fr*

Abstract:

Semiconductor alloys $ZnSn_xGe_{1-x}N_2$ have theoretical crystal structure and electronic structure similar to that of InGaN alloys. These promises of direct and tunable band gaps are very attractive to unlock a suite of functionality for these nitride semiconductors, namely for the use in long wavelength light emitters and light absorbers for solar cells. We report here a structural, electrical and optical investigation of sputtered $ZnSn_xGe_{1-x}N_2$ films for $0 \leq x \leq 1$ by gradually substituting germanium with tin. Compared to InGaN alloys which suffer from a miscibility gap and exhibit phase segregation beyond ~20% In, $ZnSn_xGe_{1-x}N_2$ form advantageously a continuous alloy for $0 \leq x \leq 1$. Its adjustable lattice parameter a (from 3.22 Å to 3.41 Å) according to Vegard's law as well as the linear variation of the vibration modes by Fourier transform infrared spectroscopy indicate that the $ZnSn_xGe_{1-x}N_2$ alloying is achievable without phase separation. The single chemical environment measured by Mössbauer spectroscopy for Sn^{4+} ions, whatever Sn content in $ZnSn_xGe_{1-x}N_2$, confirms the continuous nature of alloying. Samples exhibit semiconducting properties, including optical band gaps and electronic behaviors with temperature. The experimental observations show that the resistivity in $ZnSn_xGe_{1-x}N_2$ alloys can cover several orders of magnitude from a "quasi-metallic" (for $ZnSnN_2$) to a "quasi-insulating" (for $ZnGeN_2$) behavior and that the band gap is tunable from 2.1 eV to 3.04 eV with a nearly linear dependence on the composition. Thus, $ZnSn_xGe_{1-x}N_2$ materials offer a solution for bandgap tunability in nitride semiconductors, and may enable enhanced functionality such as efficient green and red light emitters and light absorbers for photosynthetic devices.

Keywords: Zinc tin germanium nitride alloys; Sputtering; Optical bandgaps; Tunable optical bandgap; Optoelectronic applications.

1. Introduction

InGaN-based semiconductor materials are used in current commercial colored blue and green Light Emitting Diodes (LEDs) [1]. The In content in the InGaN alloys enables tuning the band gap energy (E_g) within the range set by the two binary compounds InN (E_g=0.69 eV) and GaN (E_g=3.51 eV) and achieving the desired emission wavelength. Hence, InGaN alloys provide a class of semiconductors whose bandgap can, in principle, span the entire visible spectrum and beyond. However, the large lattice mismatch between InN and GaN results in phase segregation and the synthesis of homogeneous high quality crystals with more than 20% Indium [2,3] to produce an emission in the red range of the color

spectrum is not straightforward. Numerous works to achieve efficient red LEDs based on InGaN alloys are still ongoing. This bottleneck motivates the search for alternatives to current III-nitride semiconductors for optoelectronics applications.

The Zn-IV-N_2 compounds (where IV=Ge, Sn) closely related to the III-N compounds have similar electronics and optical properties to InGaN, as for example direct bandgaps and large optical absorption coefficients [4,5]. Those alloys appear to be analogous to III-N compounds with the group III elements (In or Ga) replaced by a combination of group II element (Zn) and a group IV element (Sn or Ge). Calculations [6-8] performed using density functional theory for the $ZnSn_xGe_{1-x}N_2$ alloys have predicted that the band gaps span the range 1.4-3.1 eV which includes the full visible spectrum. Recently, the concept of type II ZnGe(Sn)N_2/InGaN quantum well LEDs design [9-12] was proposed and revealed that the red emission can be reached with low In content (less than 20%) with an increased radiative recombination rate (better quantum efficiency) compared to the classical type I In-rich (35% In) InGaN quantum wells needed to reach the red emission [13].

We describe here the preparation of $ZnSn_xGe_{1-x}N_2$ thin films grown by reactive co-sputtering and report on their structural and optoelectronic properties. Sputtering is a technique used in research and industry to grow thin films offering a wide range of possibilities concerning the choice of the material to be deposited and the experimental conditions. Co-sputtering enables the growth of alloys from separate targets and the presence of a reactive gas such as nitrogen in the sputtering chamber makes it possible to grow nitrides. It is therefore a good technique to start the study of a rather unexplored material system such as $ZnSn_xGe_{1-x}N_2$.

2. Experimental methods

Thin film samples are deposited by reactive co-sputtering at a base pressure of 10^{-6} Pa (10^{-8} mbar) from separate Zn, Sn, and Ge targets. Each target is 99.99+% pure and the sputtering gas is 99.9999% pure nitrogen. A nitrogen flow of 30 sccm is used with a constant pressure of 1.3 Pa controlled by a gate regulation valve. The Ge target is connected to a Radio Frequency (RF) source and the Zn and Sn ones to a Direct Current (DC) source. The cathodes are confocal with a target to substrate distance of approximately 10.5 cm. The substrate-holder is a rotating inconel molyblock on which the substrates are fixed and heated at 200°C. The growth time is 45 min. By varying DC currents and RF power for each growth, films whose colors range from pale orange to dark brown are synthesized. The richest Sn samples appear metallic. Four types of substrates (glass, silicon, sapphire and GaN template substrates) are used for the subsequent analysis depending on the constraints of each characterization method. No thermal treatment or chemical etching is performed on the substrates. Under the growth conditions used, it can be safely assumed that the nature of the substrates has little influence on the thin film growth regime. The analyzes performed on the different substrates can be reasonably compared.

The sample compositions determined by energy-dispersive X-ray spectroscopy (EDX) analysis are reported in Table 1 and Fig. 1. A *quanta 600* scanning electron microscope (SEM) from *FEI* with a 100 mm^2 *AXS* detector from *Bruker* are used for the EDX analyzes. P/B-ZAF method is used to quantify the elements Zn, Ge, Sn and nitrogen at 10 kV and 20 kV at different places on the samples. An average is carried out on the two energies and at the different places. The zinc concentration is indeed 50 at% for all the samples and we see a linear variation of the Sn and Ge concentration from 0 to 50 at%. The whole range of composition of the alloy from x=0 to x=1 N_2 alloy is obtained.

Zn (A)	Sn (A)	Ge (W)	Thickness (nm)	at% Zn	at% Sn	at% Ge	x
0.07	0	115	783	51	0	49	0
0.07	0.05	90	822	52	9	39	0.2
0.06	0.09	70	811	49	22	29	0.4
0.06	0.14	45	883	49	36	15	0.7
0.07	0.19	20	1035	49	47	4	0.9
0.08	0.23	0	1200	47	53	0	1

Table 1 : DC currents and RF power applied on each of the Zn, Sn and Ge source respectively to grow $ZnSn_xGe_{1-x}N_2$ samples (time growth is 45 minutes). For all samples, Zn concentration is close to 50 at% with a progressive evolution of Ge and Sn concentration. All the composition range from x=0 to x=1 of the $ZnSn_xGe_{1-x}N_2$ alloy is obtained. Si substrates are used for EDX analysis.

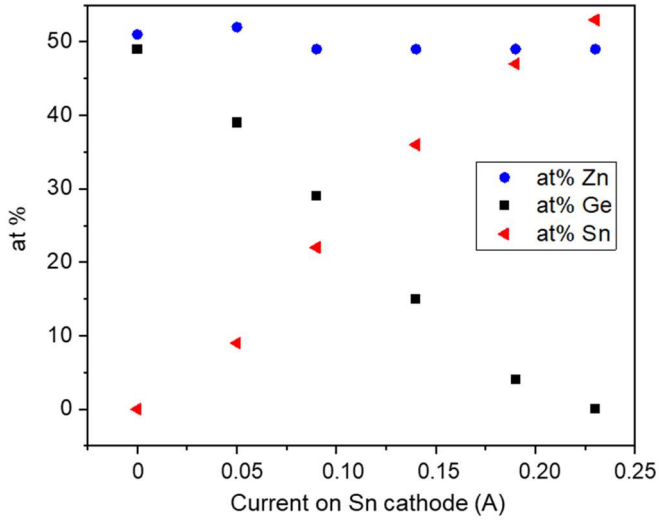

Fig. 1 : Composition of the samples (deposited on Si substrates) as a function of the current of the Sn cathode.

For cross-sectional observations of the structure of the samples, a *HITACHI S-5500* SEM is used. Atomic force microscopy (AFM) measurements are made on a *D3100* equipment from *Bruker* in TappingMode™ mode with a RTESPA-150 tip. The crystallinity of the samples is analyzed by X-ray diffraction (XRD) in Bragg-Brentano configuration (θ-2θ scans). X-ray analyses are done on a *D8 Advance* diffractometer from *Bruker* with Cu Kα radiation (λ = 1.5406 Å). Transmission electron microscopy (TEM) observations are done on a *ARM200* microscope from *Jeol*. The cross-section TEM sample preparation is made by focused ion beam (FIB) in a *Helio Nanolab 600i* SEM FIB from *FEI.* Before introduction into the FIB, sample is metallized with carbon. A Pt strip (first using electron beam then followed by ion beam) is then deposited to protect the sample before starting the milling (with Ga^+ ions) of the trench. The final sample is about 3 µm long for less than 100 nm thick. Fourier transform infrared spectroscopy (FTIR) and Raman spectroscopy methods allow to study the interatomic vibrations and the different types of bonds. FTIR spectra are acquired from 60 to 4000 cm^{-1} on a *Nicolet™ 8700 FT-IR* from *Thermo Scientific* under nitrogen flux. From 30-600 cm^{-1} the transmission spectra are acquired with a *Globar* source, a "*Solid Substrate*" type beam splitter and a *DTGS-PE* detector. From 400-4000 cm^{-1}, the transmission spectra are acquired with a *Globar* source, a *KBr* beam splitter and a *DTGS-KBr* detector (cooled with liquid nitrogen). The acquired spectra are then superimposed on the common range (400-600 cm^{-1}) in order to obtain a continuous spectrum from 60

to 4000 cm^{-1}. Raman spectroscopy is made on a *Labram HR* spectrometer from *HORIBA Jobin Yvon*. The source is a 532 nm laser, the focal length is 80 cm, the diffraction grating is 1800 or 1200 gr/µm and the CCD detector is cooled with liquid nitrogen. UV-Vis-NIR spectroscopy is used to probe the optical properties of the alloys. The measurements are made on a UV-Vis-NIR spectrophotometer, *Cary7000* from *Agilent*. Electrical measurements are made on a *K617* from *Keithley* with a two-point probe. A voltage of 100 V is applied between two coplanar electrodes (in silver paste) separated by 1 mm. The length of the electrodes is 7 mm. The sample is placed on the cold finger of a cryostat that can cover the temperature range 100-450K.

3. Results and discussion

SEM cross-sectional images (Fig. 2) give a view on the growth structure that appears columnar whatever the concentration of tin. The typical widths of the columns are of the order of 100 nm but the surface morphology of the Ge-rich columns appears to be more faceted than the Sn-rich ones, which exhibit softer domes. Different roughness parameters determined by AFM measurements on $ZnGeN_2$ and $ZnSnN_2$ films confirm these observations (Table 2). The average roughness (R_a) and the root mean squared roughness (R_q) values are clearly lower for $ZnSnN_2$ and the values of opposite sign for the skewness parameter (S_k) which characterizes the heights distribution asymmetry reveal a softer surface topography for $ZnSnN_2$. The kurtosis parameter (E_k) close to 3 measured on $ZnSnN_2$ indicates also a more rounded shape for the $ZnSnN_2$ domes.

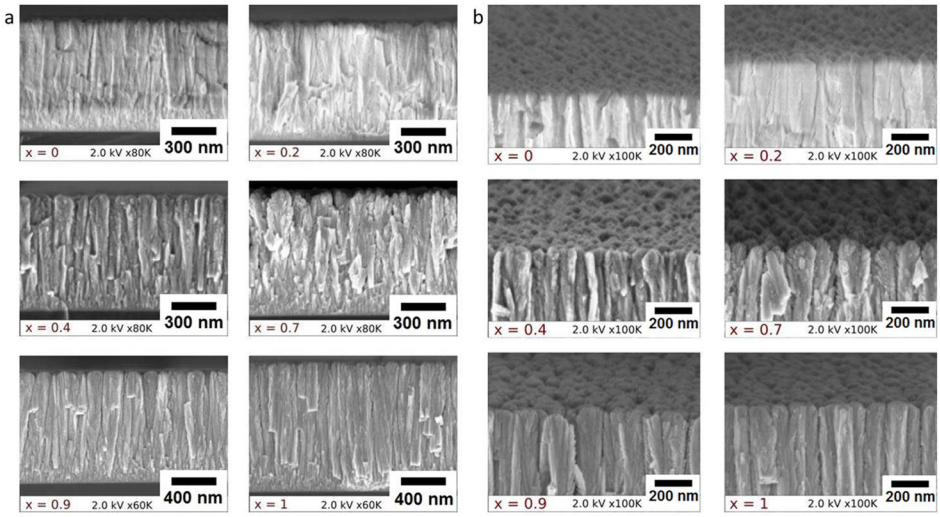

Fig. 2 : SEM images of $ZnSn_xGe_{1-x}N_2$ samples from x=0 to x=1 (deposited on Si samples). (a) Cross-sectional images. (b) Images acquired with a tilt angle of 5°.

	$ZnGeN_2$	$ZnSnN_2$
R_{max}	82 nm	53.9 nm
R_a	5.6 nm	4.8 nm
R_q	7.15 nm	6.1 nm
S_k	0.5	-0.5
E_k	4.9	3.3

Table 2 : Roughness parameters of $ZnGeN_2$ and $ZnSnN_2$ samples determined by AFM measurements. The presented parameters are maximum surface roughness (R_{max}), average surface roughness (R_a), root mean squared surface roughness (R_q), skewness (S_k) and kurtosis (E_k).

As it will be discussed below, the XRD patterns show that the $ZnGeN_2$ layer is polycrystalline without preferred crystalline orientation whereas $ZnSnN_2$ crystallizes with the preferential [001] out of plane orientation.

The combination of all these elements (SEM, AFM, XRD) tends to show that the deposit regime for $ZnGeN_2$ is situated between Zone Ic and Zone T (Fig. 3) according to the structure zone model described by Mahieu *et al*. [14]. For $ZnSnN_2$ the growth structure appears rather located in Zone II revealing a higher relative temperature T* (described as the ratio between the substrate temperature T_s and the melting point of the material T_m). However all the films are deposited at the same substrate temperature which means that the melting point of $ZnSnN_2$ should be much lower than that of $ZnGeN_2$. In addition, theoretical calculations predict a lower formation energy for $ZnSnN_2$ than for $ZnGeN_2$ [15, 16] which means that the crystalline growth synthesis of $ZnSnN_2$ is energetically less expensive than that of $ZnGeN_2$. This is in agreement with our observations shown above.

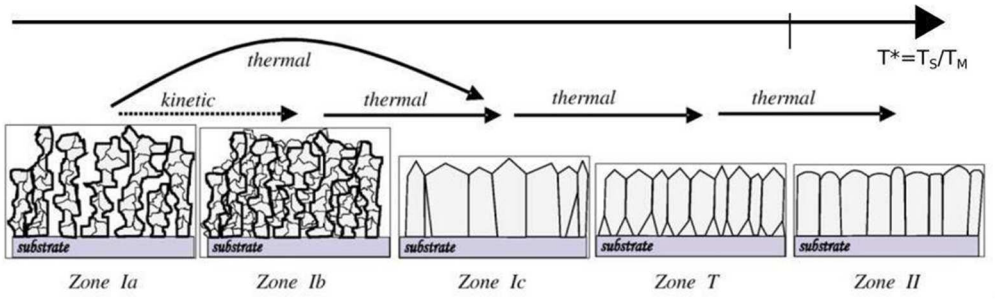

Fig. 3 : Schematic overview of the structure zone models of sputter deposited films discussed by Mahieu *et al.* The figure comes from ref [14].

Fig. 4a presents XRD θ-2θ scans for $ZnSn_xGe_{1-x}N_2$ films with various compositions grown on sapphire. Films seem to crystallize according to a hexagonal structure [4]. The three peaks (100), (002) and (101) around 2θ=35° are characteristic of this structure. $ZnSnN_2$ films appear to be better crystallized than $ZnGeN_2$ films with more intense peaks. We observe also in Fig. 4b a linear dependence in peak positions with the Sn content of the films, in agreement with Vegard's law. The deduced lattice parameters are reported in Table 3. The linear shift in Sn content indicates an apparent lack of phase separation in the material. We also observe in an evolution of the preferred crystalline orientation with Sn concentration; $ZnSnN_2$ shows a strong crystalline orientation along the c axis (presence of (002) and (004) reflections) whereas several crystalline orientations appear in $ZnGeN_2$. To quantify the degree of preferential crystalline orientation, the texture coefficient of Harris (TC) [17] is calculated and reported in Fig. 5a. [001] is indeed the preferential orientation in Sn-rich samples whereas Ge-rich samples don't seem to crystallize into a peculiar orientation. A second series of samples was fabricated exactly with the same growth conditions (Fig. 5b). Again Sn-rich films exhibit a strong preferred orientation along the [001] direction. But Ge-rich samples appear to crystallize differently from the first series. These observations are in agreement with the structure zones identified above. In the Ic-T Zone, for $ZnGeN_2$ growth, atoms merely have the needed energy to nucleate crystalline seeds. The energy supply is not enough to allow atomic diffusion from seed to seed and each grain grows along its own and initial crystalline orientation. Crystalline orientations of the Ge-rich samples appear to be random from one sample to another. With Sn incorporation, the structure zone is moving towards Zone II where atoms can diffuse from one grain to another to recrystallize the layer. The thin layer tends towards its most stable thermodynamic state with a preferential out of plane orientation, the c axis ([001] direction in our case).

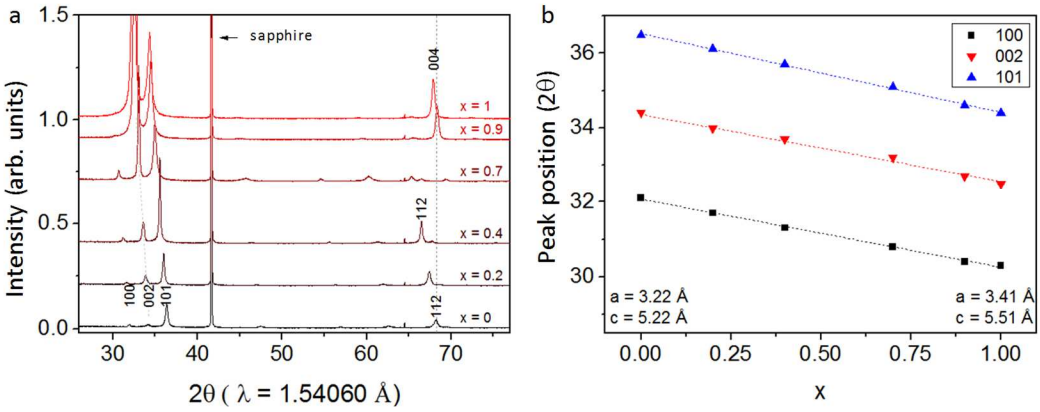

Fig. 4 : (a) XRD θ-2θ scans for $ZnSn_xGe_{1-x}N_2$ films with various compositions grown on sapphire. (b) Linear relationship between 3 peak positions ((100), (002) and (101) reflections) and the alloy composition.

x	0	0.2	0.4	0.7	0.9	1
a (Å)	3.22	3.25	3.30	3.35	3.39	3.41
c (Å)	5.22	5.27	5.32	5.40	5.47	5.51

Table 3 : Lattice parameters (a and c) of $ZnSn_xGe_{1-x}N_2$ with a hexagonal indexing.

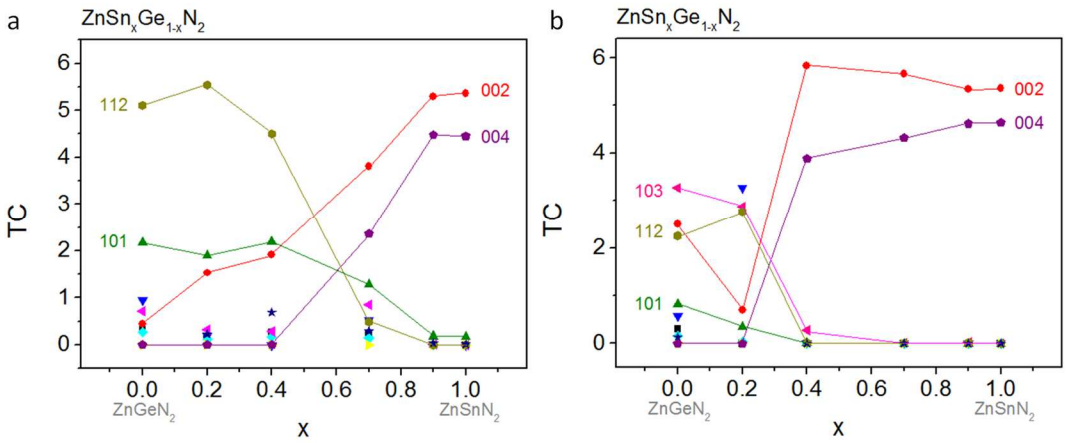

Fig. 5 : Texture coefficient of Harris (TC) calculated for 2 series of alloys (a and b) with identical deposition parameters.

Columnar grain structure, observed by SEM, was confirmed by bright-field TEM. A representative image taken from a $ZnGeN_2$ film cross section is shown in Fig. 6. The width of the columns is ranging between 50 and 80 nm on film top surface. The diffraction pattern acquired on the columnar area reveals a polycrystalline structure and matches very well the simulated diffraction pattern for a hexagonal structure with lattice parameters a=3.23 Å and c=5.25 Å. We see clearly the first three rings corresponding to (100), (002) and (101) planes, which is consistent with XRD analysis.

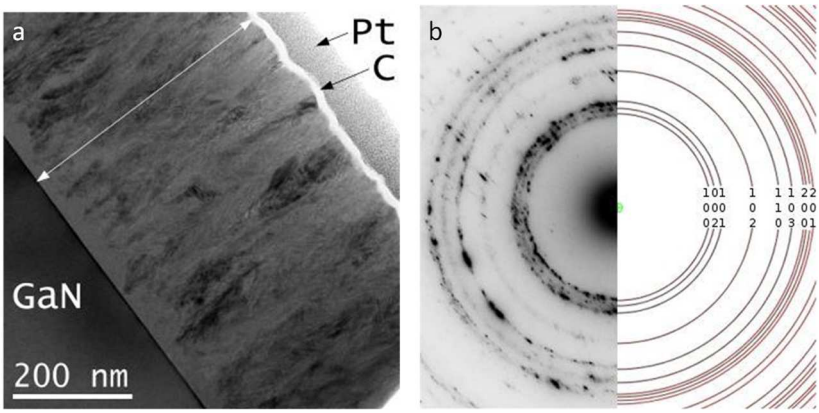

Fig. 6 : (a) Bright field TEM of a $ZnGeN_2$ film cross section deposited on GaN substrate. (b) Experimental (left) and simulated (right) diffraction pattern. A hexagonal structure with lattice parameters a=3.23 Å and c=5.25 Å is considered for the simulation.

Mössbauer spectroscopy is a powerful tool to obtain information about the chemical environment of tin atoms [18]. The Mössbauer spectra of three samples of $ZnSn_xGe_{1-x}N_2$ (with x=0.2, x=0.7 and x=1) recorded at 300 K are depicted in Fig. 7. The experimental curves are fitted with a single doublet and the values of the corresponding isomeric shift (IS) and quadripolar splitting (QS) are reported in Table 4. An IS of 1.06 mm/s is characteristic of Sn^{4+} ions in tetrahedral configuration. So, whatever the composition of the alloy, the tin appears to be located in a single crystallographic site. The decreasing value of QS with Sn content could mean a reduction in the deformation of the tetrahedrons in agreement with a better crystallinity of the Sn-rich samples with more regular and less distorted crystalline cells. These observations tend to confirm the tendency of a homogeneous nature of $Zn(Ge,Sn)N_2$ alloying.

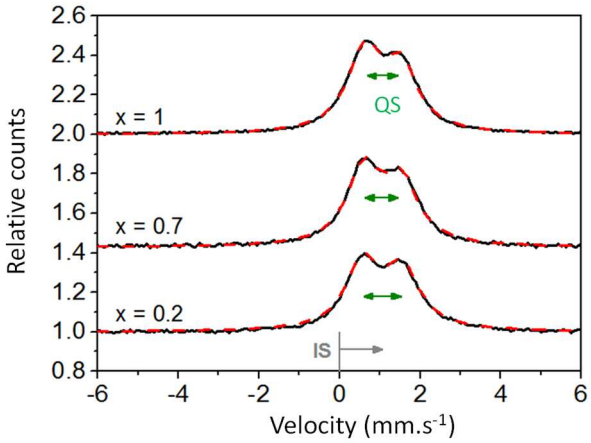

Fig. 7 : Experimental (black) and simulated (red) ^{119}Sn Mössbauer spectra of $ZnSn_xGe_{1-x}N_2$ (deposited on Si substrates).

x	IS (mm/s)	QS (mm/s)
0.2	1.06	0.97
0.7	1.06	0.93
1	1.06	0.90

Table 4 : Hyperfine parameters of $ZnSn_xGe_{1-x}N_2$ (Isomeric Shift and Quadripolar Splitting).

FTIR spectra acquired on the samples deposited on silicon substrates are reported in Fig. 8a. For all x values of $ZnSn_xGe_{1-x}N_2$, they are fitted using five Gaussians to identify the vibration modes. An

evolution of the FTIR peak positions as a function of the composition is visible in Fig. 8b. Only few studies [19,20] report on the clear analysis of FTIR peaks of $ZnGeN_2$. Shang *et al.* [19] reported 3 peak families. The peak at ~ 750 cm^{-1} can be attributed to Ge-N bonds [21]. In the case of $ZnSn_xGe_{1-x}N_2$ alloy, the progressive shift of this vibration mode towards small wavenumbers with increasing Sn content (~ 650 cm^{-1} for $ZnSnN_2$) could be the signature of the substitution of Ge atoms by heavier Sn atoms and the formation of the Sn-N bonds in the alloy. The peaks in the far IR show the same evolution, from 280 cm^{-1} to 200 cm^{-1}, and could also be attributed to a Ge-N bond evolving towards a Sn-N bond. The less pronounced evolution (< 50 cm^{-1}) of the vibration mode at ~ 600 cm^{-1} seems consistent with the hypothesis of a Zn-N-Ge bond [16] changing to Zn-N-Sn bond during the formation of the quaternary alloy. Finally, the peak at ~ 500 cm^{-1} attributed to Zn-N [22] bond shouldn't change in position in the $ZnSn_xGe_{1-x}N_2$ material. But it also appears to shift slightly towards smaller wavenumbers with increasing Sn content. In presence of tin, it can be assumed that the different chemical environment can cause a progressive shift of the Zn-N vibration mode.

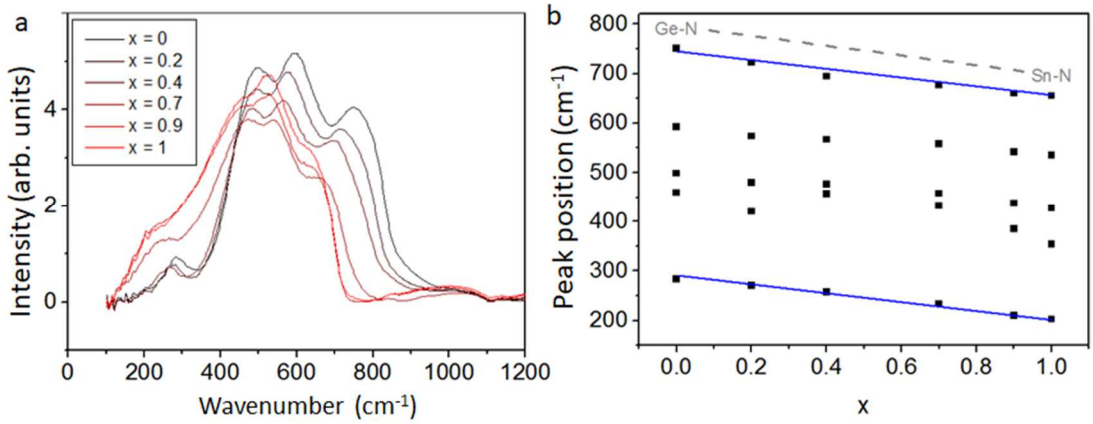

Fig. 8 : (a) Plots of the FTIR measurements for $ZnSn_xGe_{1-x}N_2$ (deposited on Si samples). (b) Evolution of the FTIR peak positions as a function of the composition.

Raman spectroscopy on the different alloys tends to support this behavior as displayed on Fig. 9. The optical modes shift towards the low frequencies when heavier Sn atoms are substituted to Ge in the alloy. This is consistent with previous FTIR measurements. The Raman peaks don't appear well defined. The sputtered alloys rather have the signature of a phonon-glass-like revealing densities of state widen by defects and disorder. The phonon densities of state calculated by Paudel *et al.* [16] for $ZnGeN_2$ and $ZnSnN_2$ crystals are reported in Fig. 10 (a and d). To compare with experimental data, Lambrecht *et al.* [23] simulate the Raman spectra by convoluting the spectra with a Gaussian broadening (Fig. 10b and e). The spectra consist of three main regions, a region which is basically a folding of the acoustic branch (between 130 and 340 cm^{-1} for $ZnGeN_2$ and between 100 and 280 cm^{-1} for $ZnSnN_2$), a lower optical branch, called the transverse optic region (between 470 and 700 cm^{-1} for $ZnGeN_2$ and between 430 and 640 cm^{-1} for $ZnSnN_2$) and an upper optical branch we are tempted to call longitudinal optic region (between 760 and 860 cm^{-1} for $ZnGeN_2$ and between 660 and 750 cm^{-1} for $ZnSnN_2$). The low frequency region contains two peaks which can be correlated with the corresponding experimental peaks at about 130 cm^{-1} and 275 cm^{-1} for $ZnGeN_2$ (respectively 100 cm^{-1} and 230 cm^{-1} for $ZnSnN_2$). According to Lambrecht *et al.* [23], the second experimental peak appears higher in intensity in part because there is a strong overlap with the second harmonics of the first peaks. Our experimental spectra for $ZnGeN_2$ and $ZnSnN_2$ are reported for comparison once again in Fig. 10 (c and f). The next broad region shows three peaks in the theory for $ZnGeN_2$, 480, 560 and 660 cm^{-1}. In the experiment, one sees a broader spectrum with very little pronounced modes at 465, 540, 650 cm^{-1}. However for $ZnSnN_2$, the two

predicted peaks at 470 and 590 cm^{-1} can be easily correlated to the two experimental peaks observed in the 400-600 cm^{-1} region. Finally, at higher frequency we find a peak at about 780 cm^{-1} for $ZnGeN_2$ while the experiment shows a peak at 800 cm^{-1}. For $ZnSnN_2$, the theoretical peak is predicted to be at 700 cm^{-1} while the experimental spectrum shows a peak at 655 cm^{-1}. Given the complexity of the spectra and the difficulty in identifying the modes in our polycrystalline samples, the agreement between experiment and theory is rather satisfactory. The Raman spectrum of $ZnSnN_2$ shows better resolved optical modes than $ZnGeN_2$ revealing a better crystal quality of the samples, which is consistent with the previous XRD measurements.

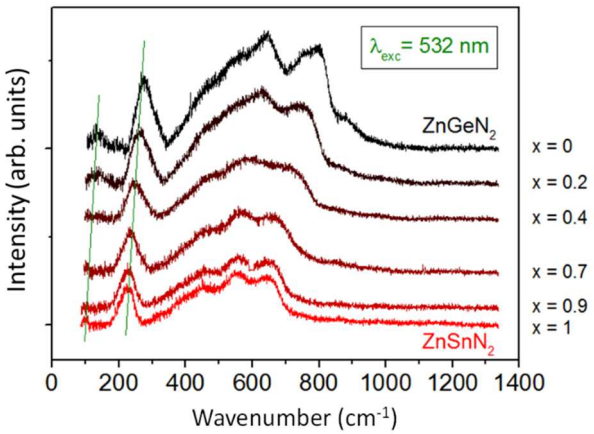

Fig. 9 : Measured Raman spectra for $ZnSn_xGe_{1-x}N_2$ (deposited on Si samples).

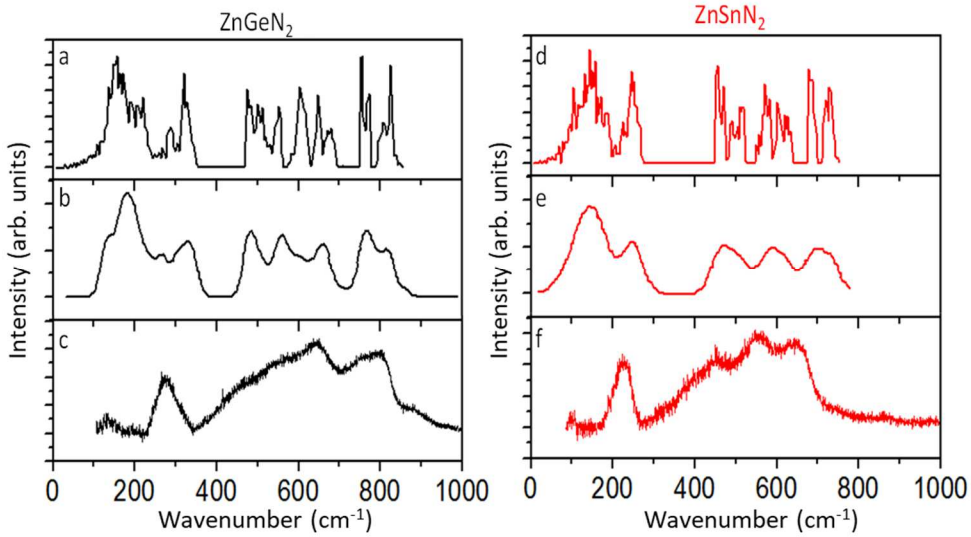

Fig. 10 : Raman spectra and calculated phonon density of states of $ZnGeN_2$ and $ZnSnN_2$. (a) and (d) Calculated density of states according to Paudel *et al.* [16] and Lambrecht *et al.* [23] (b) and (e) Calculated density of states: Gaussian broadened. (c) and (f) our measured Raman spectra.

In agreement with previous papers [24-26], the results presented above highlight the continuous nature of $ZnSn_xGe_{1-x}N_2$ alloying films for $0 \leq x \leq 1$. The linear evolution of the lattice parameters according to Vegard's law, the linear variation of the position of the different chemical bonds identified by FTIR spectroscopy and the continuous evolution of the Raman modes indicate a progressive substitution of Ge by Sn without phase separation.

Fig. 11a shows the dependence of the resistivity measured on the $ZnSn_xGe_{1-x}N_2$ samples deposited on glass substrates and measured at 120, 300 and 420K using a two-point probe. $ZnGeN_2$ sample exhibits a resistivity of 2.10^9 Ω.cm (at 300 K) while $ZnSnN_2$ sample shows a resistivity of several order of magnitude lower (30 Ω.cm). Thus, an increase in the Sn content produces a strong decrease in the resistivity of the $ZnSn_xGe_{1-x}N_2$ alloys. Ge-rich $ZnSn_xGe_{1-x}N_2$ samples ($0 \leq x \leq 0.5$) exhibit a typical semi-conducting behavior with an almost exponential increase in resistivity as temperature decreases. Typically, the resistivity of $ZnGeN_2$ varies on several orders of magnitude, between 7.10^5 Ω.cm and 4.10^{10} Ω.cm when temperature decreases from 400 to 120 K. This behavior is consistent with the insulating character previously reported for sputtered $ZnGeN_2$ films [27]. On the contrary, $ZnSnN_2$ shows a rather "metallic" behavior; its resistivity barely changes with temperature (but shows a slight and linear increase as the temperature decreases) and is of the order of 30 Ω.cm. The strong decrease in resistivity with increased Sn concentration can be attributed to a decrease in the band gap (as discussed in the next paragraph) and to an increase in the number of thermally activated carriers in the conduction band of the alloys. Furthermore, the substitution of Ge by Sn may increase the number of electrons available for conduction because Sn is less electronegative than Ge and hence Sn is a better electron donor than Ge. The presence of small grains (less than 100 nm), grain boundaries and defects in sputtered samples likely dominates the mobility term. And thus the resistivity of the samples reflects the carrier concentrations in the films.

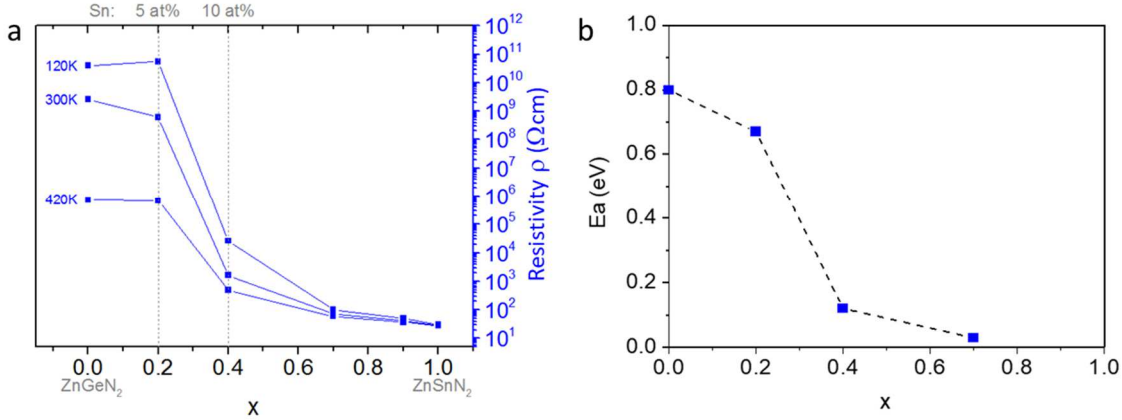

Fig. 11 : (a) Resistivity of $ZnSn_xGe_{1-x}N_2$ thin films (deposited on glass) and measured at 3 temperatures (120, 300 and 420 K). (b) Activation energies corresponding to the slope of the linearly fitted part of Arrhenius plots (log of resistivity versus inverse temperature).

Other groups report the resistivity values of sputtered $ZnSn_xGe_{1-x}N_2$ alloys [24]. They observe the same tendencies with Sn content and temperature but measure different absolute values for resistivity. For example, samples prepared by Shing *et al.* [24] with the same Sn concentration show a much lower resistivity than ours (for example, for x=0.4, we measure a resistivity of 10^3 Ω.cm and Shing *et al.* report a resistivity of about 10 Ω.cm). Alnjiman *et al.* [18] report values of 0.23 Ω.cm for highly crystallized $ZnSnN_2$ samples and Fioretti *et al.* [28] obtain a resistivity in the 0.03 and 50 Ω.cm range. These differences in resistivity appear to be strongly dependent on the sputtering conditions used. The final composition, microstructure of the samples and their crystal quality are undoubtedly key factors.

Arrhenius plots (log of resistivity versus inverse temperature) were plotted for the samples (not shown here). For $0 \leq x \leq 0.7$, the slopes of the linearly fitted data yielded activation energies E_a for the carriers. According to the discussion above and according to Hall measurements described in literature, it seems reasonable to think that $ZnSn_xGe_{1-x}N_2$ alloys are intrinsically n-doped materials [4,18,28,29]. Hence, E_a corresponds to the difference in energy between the Fermi level and the bottom of the conduction

band. The evolution of E_a is shown in Fig. 11b. E_a decreases for increasing x values until it becomes difficult to determine above x = 0.7 because the resistivity of tin-rich samples decreases very rapidly. A low E_a means that the majority charge carriers (electrons in our case) fill states very close of the conduction band. The decrease in activation energy as the Sn content increases agrees with the higher conductivity observed for the Sn-rich samples, consistent with a reduced activation energy required for thermal excitation of carriers into the conduction band.

UV-Vis-NIR transmittance and reflectance measurements were used to probe the optical properties of the alloys. In the visible part of the spectrum, the incorporation of Sn in the alloy induces a red shift in the transmission onset compared to $ZnGeN_2$ thin films (Fig. 12a). As it will be discussed in the next paragraph, this behavior is related to a shift in absorption into the red region with bandgap energies smaller for Sn-rich alloys compared to Ge-rich alloys. A focus in the IR region (λ>1000 nm) shows that the sum of the transmittance and reflectance measurements is close to 100% for the Ge-rich samples (Fig. 12b). So there is no absorption below the bandgap of the alloy. But for Sn-rich samples, T+R is less than 100%, revealing a strong absorption phenomenon below the gap (at $\lambda \sim 2250$ nm for $ZnSnN_2$). This absorption may be due to the presence of free carriers in Sn rich samples (as discussed above) and give rise to plasmon resonance effects. From equation 1 describing the plasmon frequency [30]:

$$\lambda_p = 2\pi c \left(\frac{\varepsilon_0 m^*}{Ne^2}\right)^{1/2} \quad (1)$$

where N is the free carrier density and m* the free carrier effective mass, ε_0 the vacuum permittivity, c the speed of light, we can determine the corresponding value of the free carrier density for $ZnSnN_2$. An electron concentration N in the $3.10^{19} - 2.10^{20}$ cm^{-3} range is obtained (for $0.15m_e<m^*<1m_e$ where m_e is the mass of the free electron and $0.15m_e$ is the calculated effective mass for electrons in $ZnSnN_2$ [5]).

These values are consistent with the ones determined by Hall Effect measurements on sputtered $ZnSnN_2$) [4, 18, 28].

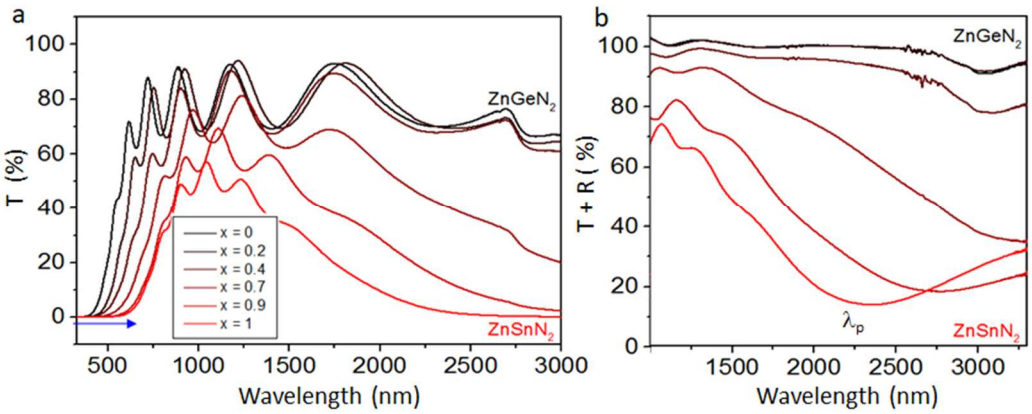

Fig. 12 : (a) Transmittance (T) of the $ZnSn_xGe_{1-x}N_2$ films (deposited on sapphire substrates) in the UV-visible-SWIR range. The arrow in the visible part of the spectrum indicates the red shift in the transmittance as the Sn content increases. (b) Transmittance (T) + Reflectance (R) in the SWIR range. λ_p reveals a plasmon resonance in $ZnSnN_2$ in the IR region.

To investigate the optical properties of the alloys, particularly close to the absorption onset of the materials, we plot the absorption coefficient α (not shown here) deduced from UV/Vis transmittance data by the equation $\alpha = -1 / d \ln (T_{film})$, with *d* the film thickness and $T_{film} \sim T_{experimental}/T_{susbtrate}$. The absorption exhibits an obvious red shift as the Sn composition increases. For direct band gap

semiconductors, the value of the band gap can be estimated by linear extrapolation to the energy axis of a plot of the square of αE (where α is the absorption coefficient and E the photon energy) versus E. The fitted gaps are 2.12 eV for $ZnSnN_2$ and 3.04 eV for $ZnGeN_2$. But the rather soft Tauc plots allow only a subjective determination of the gaps with uncertainties expressed by the error bars in Fig. 13. Despite these uncertainties in the exact values of the gaps, it is safe to say that the gap is around 2.0 eV for $ZnSnN_2$ and that of $ZnGeN_2$ is around 3.1 eV. These values are close to those measured by other groups for sputtered films, around 2 eV for $ZnSnN_2$ [4,18,31] and around 3.1 eV for $ZnGeN_2$ [32]. Fig. 13 shows the change in optical band gap as a function of composition, with the band gap ranging from 2 to 3 eV and thereby allowing access to the entire bandgaps between $ZnSnN_2$ and $ZnGeN_2$. To investigate the band gap bowing of the $ZnSn_xGe_{1-x}N_2$ alloy, the determination of the optical gap E_{04} [33], corresponding to $\alpha=10^{-4}$ cm^{-1} is more robust and its variation as a function of the composition x is shown in Fig. 14. The bandgap E_{04} depends nearly linearly on the composition x, as evidenced by the bowing parameter *b*, defined as: $E_{04}(x) = x\ E_{04}(1) + (1-x)\ E_{04}(0) - b\ x\ (1-x)$ where $E_{04}(1)$ is the E_{04} gap value of $ZnSnN_2$ and $E_{04}(0)$ is the E_{04} gap value of $ZnGeN_2$. A bowing parameter of b = 0.87 eV is determined from the measured bandgaps of $ZnSn_xGe_{1-x}N_2$. This value is higher than the ones experimentally determined (b = 0.29 eV) and theoretically calculated (b = 0.67 eV) by Narang *et al.* [31] Despite this difference, *b* values are significantly smaller than *b* for the $In_{1-x}Ga_xN$ alloy (b = 1.43 eV) [34]. The small value of *b* means that the $ZnSn_xGe_{1-x}N_2$ alloy bandgaps can be tuned almost linearly by controlling the Sn/Ge composition.

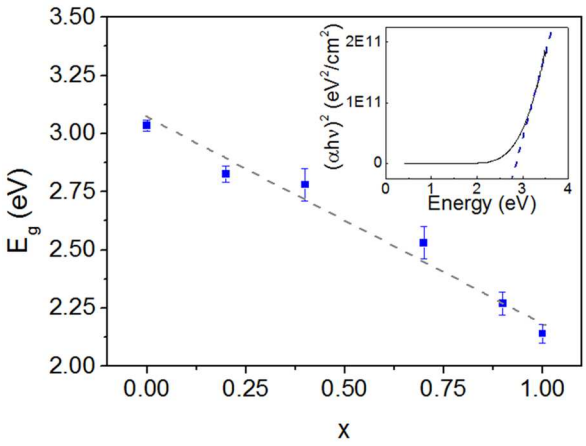

Fig. 13 : Dependence of the optical band gap E_g of the $ZnSn_xGe_{1-x}N_2$ films. The inset corresponds to the Tauc plot to determine the band gap of $ZnGeN_2$. The rather soft Tauc plots obtained on the other compositions allow only a subjective determination of the gap with uncertainties expressed by the error bars.

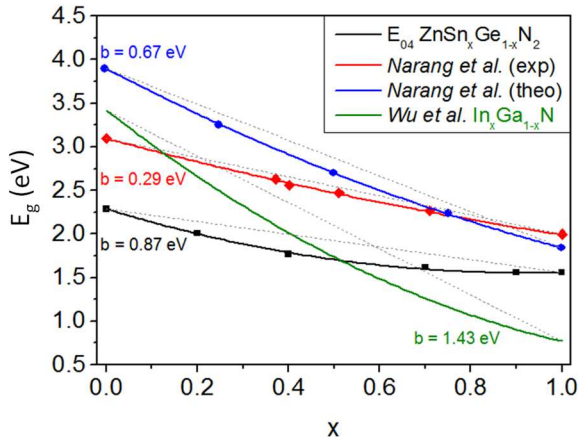

Fig. 14 : Bowing parameter *b* determined from the measured E_{04} bandgaps of $ZnSn_xGe_{1-x}N_2$ (black curve). The red and blue curves correspond to the values determined experimentally and theoretically by Narang *et al*. [31]. The green curve shows the band gap bowing for $In_xGa_{1-x}N$ reported by Wu *et al.* [34].

4. Conclusions

In this work, we have presented a structural, electrical and optical investigation of the $ZnSn_xGe_{1-x}N_2$ for $0 \leq x \leq 1$ by gradually substituting germanium with tin. Films are fabricated using reactive sputtering. Compared to InGaN alloys which are difficult to synthetize as homogeneous alloys, without phase segregation, across the full range of [In]/[Ga] ratio, $ZnSn_xGe_{1-x}N_2$ seem to form advantageously a continuous alloy for $0 \leq x \leq 1$. The linear evolution of the lattice parameters according Vegard's law as well as the linear variation of the peak positions of the different vibration modes identified by FTIR spectroscopy indicate that the $ZnSn_xGe_{1-x}N_2$ alloying is achievable without phase separation. Moreover, whatever Sn content in $ZnSnGeN_2$, Mössbauer spectroscopy, evidences that tin ions are Sn^{4+} ions in a single tetrahedral configuration and confirms the continuous nature of alloying. Samples exhibit semiconducting properties, including optical band gaps and decreasing in resistivities with temperature. The resistivities of $ZnSnN_2$ are a few tenths of Ω.cm and resistivities of $ZnSn_xGe_{1-x}N_2$ alloys increased exponentially with decreased Sn content, whereas sputtered $ZnGeN_2$ thin film exhibited a quasi-insulating behavior. The experimental observations have also shown that the band gap in $ZnSn_xGe_{1-x}N_2$ is tunable from 2.1 eV to 3.04 eV with a nearly linear dependence on the composition. Thus, $ZnSn_xGe_{1-x}N_2$ materials offer a solution for bandgap tunability in nitride semiconductors, and may enable enhanced functionality such as long wavelength (green and red) light emitters and light absorbers for solar cells. To enable these future applications, additional experimental work on doping and band offset in alloys will be needed to move towards device integration where theoretical works have already suggested promising optoelectronic device architectures with tunable wavelengths.

Acknowledgements

This work was funded by the Région Lorraine and the European Regional Development Fund.

Patrice Miska passed away in November 2018 before we finished to write this article. We have done our best with respect to his memory.

References

[1] M. H. Crawford, LEDs for Solid-State Lighting: Performance Challenges and Recent Advances, IEEE J. Sel. Top. Quantum Electron. 15 (2009) 1028-1040.

[2] N. Duxbury, U. Bangert, P. Dawson, E. J. Thrush, W. Van der Stricht, K. Jacobs, I. Moerman, Indium segregation in InGaN quantum-well structures, Appl. Phys. Lett. 76 (2000) 1600-1602.

[3] Z. Liliental-Weber, D. N. Zakharov, K. M. Yu, J. W. Ager, W. Walukiewicz, E. E. Haller, H. Lu, W. J. Schaff, Compositional modulation in $In_xGa_{1-x}N$: TEM and X-ray studies, J. Electron Microsc. 54 (2005) 243-250.

[4] L. Lahourcade, N. C. Coronel, K. T. Delaney, S. K. Shukla, N. A. Spaldin, H. A. Atwater, Structural and optoelectronic characterization of RF sputtered $ZnSnN_2$, Adv. Mater. 25 (2013) 2562-2565.

[5] A. Punya, W. R. L. Lambrecht, M. van Schilfgaarde, Quasiparticle band structure of Zn-IV-N_2 compounds, Phys. Rev. B 84 (2011) 165204.

[6] A. Punya, T. R. Paudel, W. R. L. Lambrecht, Electronic and lattice dynamical properties of II-IV-N_2 semiconductors, Phys. Status Solidi C 8 (2011) 2492-2499.

[7] S. Limpijumnong, S. N. Rashkeev, W. R. L. Lambrecht, Electronic Structure and Optical Properties of $ZnGeN_2$, MRS Internet J. Nitride Semicond. Res. 4, (1999) 600-605.

[8] A. Punya, W. R. L. Lambrecht, Band offsets between $ZnGeN_2$, GaN, ZnO, and $ZnSnN_2$ and their potential impact for solar cells, Phys. Rev. B 88 (2013) 075302.

[9] L. Han, K. Kash, H. Zhao, Designs of blue and green light-emitting diodes based on type-II InGaN-$ZnGeN_2$ quantum wells, J. Appl. Phys. 120 (2016) 103102.

[10] M. Rolles, B. Hyot, P. Miska, New Architecture of $ZnGeN_2$/$In_{0.16}Ga_{0.84}N$ Type-II Quantum Well-Based Green Emitting LED, Phys. Status Solidi - Rapid Res. Lett. 12 (2018) 1800173.

[11] M. Rolles, B. Hyot, P. Miska, Design of Efficient Type-II $ZnGeN_2$/$In_{0.16}Ga_{0.84}N$ Quantum Well-Based Red LEDs, Phys. Status Solidi - Rapid Res. Lett. (2019) 1900170.

[12] A. Gorai, Red light emitting diodes based on the type-II InGaN-$ZnSnN_2$/GaN quantum wells, Mat. Sci. Semicon. Proc. 82 (2018) 25-30.

[13] J. I. Hwang, R. Hashimoto, S. Saito, S. Nunoue, Development of InGaN-based red LED grown on (0001) polar surface, Appl. Phys. Express 7 (2014) 071003.

[14] S. Mahieu, P. Ghekiere, D. Depla, R. De Gryse, Biaxial alignment in sputter deposited thin films, Thin Solid Films 515 (2006) 1229-1249.

[15] W. R. L. Lambrecht, A. Punya, Heterovalent ternary II-IV-N_2 compounds: perspectives for a new class of wide-band-gap nitrides, Chap 15 in: III-Nitride Semiconductors and their Modern Devices, B. Gil (Ed.) 2013, pp. 519-585. ISBN-13: 9780199681723

[16] T. R. Paudel, W. R. L. Lambrecht, First-principles study of phonons and related ground-state properties and spectra in Zn-IV-N_2 compounds, Phys. Rev. B 78 (2008) 115204.

[17] C. V. Manzano, A. A. Rojas, M. Decepida, B. Abad, Y. Feliz, O. Caballero-Calero, D. A. Borca-Tasciuc, M. Martin-Gonzalez, Thermoelectric properties of Bi_2Te_3 films by constant and pulsed electrodeposition, J Solid State Electr 17 (2013) 2071-2078.

[18] F. Alnjiman, S. Diliberto, J. Ghanbaja, E. Haye, S. Kassavetis, P. Patsalas, C. Gendarme, S. Bruyère, F. Cleymand, P. Miska, P. Boulet, J.F. Pierson, Chemical environment and functional properties of highly crystalline $ZnSnN_2$ thin films deposited by reactive sputtering at room temperature, Sol. Energy Mater. Sol. Cells 182 (2018) 30-36.

[19] M. Shang, J. Wang, J. Fan, H. Lian, Y. Zhang, J. Lin, $ZnGeN_2$ and $ZnGeN_2$:Mn^{2+} phosphors: hydrothermal-ammonolysis synthesis, structure and luminescence properties, J. Mater. Chem. C 3, (2015) 9306-9317.

[20] N. Beddelem, N. Rochat, C. Licitra, B. Hyot, P. Miska, Study of amorphous Zinc Germanium Nitride thin films grown by reactive co-sputtering, J. Non-Cryst. Solids 482 (2018) 132-136.

[21] A. R. Zanatta, I. Chambouleyron, Nitrogen in the amorphous-germanium network: From high dilution to the alloy phase, Phys. Rev. B 48 (1993) 4560-4570.

[22] S. Nazir, J. Anwar, M. A. Munawar, Synthesis and characterization of zinc and cadmium complexes with deoxyalliin, J. Chem. Soc. Pak. 31 (4) (2009) 614-621.

[23] W. R. L. Lambrecht, E. Alldredge, K. Kim, Structure and phonons of $ZnGeN_2$, Phys. Rev. B 72, (2005) 155202.

[24] A. M. Shing, N. C. Coronel, N. S. Lewis, H. A. Atwater, Semiconducting $ZnSn_xGe_{1-x}N_2$ alloys prepared by reactive radio-frequency sputtering, APL Mater. 3 (2015) 076104.

[25] N. C. Coronel, L. Lahourcade, K. T. Delaney, A. M. Shing, H. A. Atwater, Earth-abundant $ZnSn_xGe_{1-x}N_2$ alloys as potential photovoltaic absorber materials, 38th IEEE Photovoltaic Specialists Conference, PVSC (2012). DOI: 10.1109/PVSC.2012.6318259

[26] A. M. Shing, N. C. Coronel, N. S. Lewis, H. A. Atwater, Fabrication and characterization of $ZnSn_xGe_{1-x}N_2$ Alloys for light absorbers, 42nd IEEE Photovoltaic Specialist Conference, PVSC (2015). DOI: 10.1109/PVSC.2015.7355918

[27] T. Misaki, A. Wakahara, H. Okada, A. Yoshida, Epitaxial growth and characterization of $ZnGeN_2$ by metalorganic vapor phase epitaxy, J. Cryst. Growth 260 (2004) 125-129.

[28] A. N. Fioretti, A. Zakutayev, H. Moutinho, C. Melamed, J. D. Perkins, A. G. Norman, M Al-Jassim, E. S. Toberer, A. C. Tamboli, Combinatorial insights into doping control and transport properties of zinc tin nitride, J. Mater. Chem C. 3 (2015) 11017-11028.

[29] R. Qin, H. Cao, L. Liang, Y. Xie, F. Zhuge, H. Zhang, J. Gao, K. Javaid, C. Liu, W. Sun, Semiconducting $ZnSnN_2$ thin films for Si/$ZnSnN_2$ p-n junctions, Appl. Phys. Lett. 108 (2016) 142104.

[30] M. Jullien, D. Horwat, F. Manzeh, R. Escobar Galindo, P. Bauer, J. Pierson, J. Endrino, Influence of the nanoscale structural features on the properties and electronic structure of Al-doped ZnO thin films: an X-ray absorption study, Sol. Energy 95 (2011) 2341.

[31] P. Narang, S. Chen, N. C. Coronel, S. Gul, J. Yano, L-W Wang, N. S. Lewis, H. A. Atwater, Bandgap tunability in Zn(Sn,Ge)N(2) semiconductor alloys, Adv. Mater. 26 (2014) 1235-1241.

[32] S. Kikkawa, H. Morisaka, RF-sputter deposition of Zn–Ge nitride thin films, Solid State Commun., 112 (9) (1999) 513-515.

[33] O. Stenzel, Oxide Coatings: Porous and Dense Films, Chap. 7 in: Optical Coatings - Material Aspects in Theory and Practice, Springer Berlin Heidelberg, Berlin, Heidelberg, 2014, pp. 187-208. ISBN 978-3-642-54063-9.

[34] J. Wu, W. Walukiewicz, K. M. Yu, J. W. Ager, E. E. Haller, H. Lu, W. J. Schaff, Small band gap bowing in $In_{1-x}Ga_xN$ alloys, Appl. Phys. Lett., 80 (25) (2002) 4741-4743.

Figure captions:

Fig. 1 : Composition of the samples (deposited on Si substrates) as a function of the current of the Sn cathode.

Fig. 2 : SEM images of $ZnSn_xGe_{1-x}N_2$ samples from x=0 to x=1 (deposited on Si samples). (a) Cross-sectional images. (b) Images acquired with a tilt angle of 5°.

Fig. 3 : Schematic overview of the structure zone models of sputter deposited films discussed by Mahieu *et al.* The figure comes from ref [14].

Fig. 4 : (a) XRD θ-2θ scans for $ZnSn_xGe_{1-x}N_2$ films with various compositions grown on sapphire. (b) Linear relationship between 3 peak positions ((100), (002) and (101) reflections) and the alloy composition.

Fig. 5 : Texture coefficient of Harris (TC) calculated for 2 series of alloys (a and b) with identical deposition parameters.

Fig. 6 : (a) Bright field TEM of a $ZnGeN_2$ film cross section deposited on GaN substrate. (b) Experimental (left) and simulated (right) diffraction pattern. A hexagonal structure with lattice parameters a=3.23 Å and c=5.25 Å is considered for the simulation.

Fig. 7 : Experimental (black) and simulated (red) ^{119}Sn Mössbauer spectra of $ZnSn_xGe_{1-x}N_2$ (deposited on Si substrates).

Fig. 8 : (a) Plots of the FTIR measurements for $ZnSn_xGe_{1-x}N_2$ (deposited on Si samples). (b) Evolution of the FTIR peak positions as a function of the composition.

Fig. 9 : Measured Raman spectra for $ZnSn_xGe_{1-x}N_2$ (deposited on Si samples).

Fig. 10 : Raman spectra and calculated phonon density of states of $ZnGeN_2$ and $ZnSnN_2$. (a) and (d) Calculated density of states according to Paudel *et al.* [16] and Lambrecht *et al.* [23] (b) and (e) Calculated density of states: Gaussian broadened. (c) and (f) our measured Raman spectra.

Fig. 11 : (a) Resistivity of $ZnSn_xGe_{1-x}N_2$ thin films (deposited on glass) and measured at 3 temperatures (120, 300 and 420 K). (b) Activation energies corresponding to the slope of the linearly fitted part of Arrhenius plots (log of resistivity versus inverse temperature).

Fig. 12 : (a) Transmittance (T) of the $ZnSn_xGe_{1-x}N_2$ films (deposited on sapphire substrates) in the UV-visible-SWIR range. The arrow in the visible part of the spectrum indicates the red shift in the transmittance as the Sn content increases. (b) Transmittance (T) + Reflectance (R) in the SWIR range. λ_p reveals a plasmon resonance in $ZnSnN_2$ in the IR region.

Fig. 13 : Dependence of the optical band gap E_g of the $ZnSn_xGe_{1-x}N_2$ films. The inset corresponds to the Tauc plot to determine the band gap of $ZnGeN_2$. The rather soft Tauc plots obtained on the other compositions allow only a subjective determination of the gap with uncertainties expressed by the error bars.

Fig. 14 : Bowing parameter *b* determined from the measured E_{04} bandgaps of $ZnSn_xGe_{1-x}N_2$ (black curve). The red and blue curves correspond to the values determined experimentally and theoretically by Narang *et al*. [31]. The green curve shows the band gap bowing for $In_xGa_{1-x}N$ reported by Wu *et al.* [34].

Table captions:

Table 1 : DC currents and RF power applied on each of the Zn, Sn and Ge source respectively to grow $ZnSn_xGe_{1-x}N_2$ samples. For all samples, Zn concentration is close to 50 at% with a progressive evolution of Ge and Sn concentration. All the composition range from x=0 to x=1 of the $ZnSn_xGe_{1-x}N_2$ alloy is obtained. Si substrates are used for EDX analysis.

Table 2 : Roughness parameters of $ZnGeN_2$ and $ZnSnN_2$ samples determined by AFM measurements. The presented parameters are maximum surface roughness (R_{max}), average surface roughness (R_a), root mean squared surface roughness (R_q), skewness (S_k) and kurtosis (E_k).

Table 3 : Lattice parameters (a and c) of $ZnSn_xGe_{1-x}N_2$ with a hexagonal indexing.

Table 4 : Hyperfine parameters of $ZnSn_xGe_{1-x}N_2$ (Isomeric Shift and Quadripolar Splitting).